

# Organic Light-Emitting Transistors in a Smart-Integrated System for Plasmonic-Based Sensing

Mario Prosa,\* Emilia Benvenuti, David Kallweit, Paola Pellacani, Michael Toerker, Margherita Bolognesi, Laura Lopez-Sanchez, Vincenzo Ragona, Franco Marabelli, and Stefano Toffanin\*

The smart integration of multiple devices in a single functional unit is boosting the advent of compact optical sensors for on-site analysis. Nevertheless, the development of miniaturized and cost-effective plasmonic sensors is hampered by the strict angular constraints of the detection scheme, which are fulfilled through bulky optical components. Here, an ultracompact system for plasmonic-sensing is demonstrated by the smart integration of an organic light-emitting transistor (OLET), an organic photodiode (OPD), and a nanostructured plasmonic grating (NPG). The potential of OLETs, as planar multielectrode devices with inherent micrometer-wide emission areas, offers the pioneer incorporation of an OPD onto the source electrode to obtain a monolithic photonic module endowed with light-emitting and light-detection characteristics at unprecedented lateral proximity of them. This approach enables the exploitation of the angle-dependent sensing of the NPG in a miniaturized system based on low-cost components, in which a reflective detection is enabled by the elegant fabrication of the NPG onto the encapsulation glass of the photonic module. The most effective layout of integration is unraveled by an advanced simulation tool, which allows obtaining an optics-less plasmonic system able to perform a quantitative detection up to  $10^{-2}$  RIU at a sensor size as low as  $0.1 \text{ cm}^3$ .

## 1. Introduction

The continuous growth of the global population has been remarking the need of early detection systems to prevent the spread of epidemics as well as to improve the standards of living. The emerging demand of sensing technologies has prompted researchers and industrial companies to develop devices able to monitor medical, food, water, and environmental safety/quality indicators in an efficient, simple, and reliable way.<sup>[1]</sup> While high sensitivity and selectivity must be guaranteed, compactness, user-friendliness, and low-cost are key characteristics to enable the use of the sensing technology for point-of-care diagnostics without the need for trained personnel.<sup>[2]</sup>

Among state-of-the-art methodologies, optical sensing has emerged as one of the most simple, versatile, and powerful approaches for analytical purposes. However, a major obstacle toward the development of a portable system has been the use of bulky optical components (e.g., lasers and optical fibers), which are necessary to ensure a good sensing capability.<sup>[3]</sup> There have been several efforts to replace traditional light sources with more compact ones. For instance, light-emitting diodes (LEDs) have been used in an ultracompact biosensor operating without additional optical elements.<sup>[4]</sup> However, despite the great progress made, LEDs suffer of self-heating effects, their alignment within the whole sensor platform is often moderately difficult, and their manufacturing is also expensive.<sup>[5]</sup>

In this context, organic electronics has been establishing a leading role as a cutting-edge technology in many different fields for the possibility to obtain nanometer-thick devices at lower costs with respect to the inorganic counterpart.<sup>[6–8]</sup> The fascinating possibility to tune the optoelectronic characteristics via targeted design, synthesis, and processing of the molecular compounds provides also outstanding versatility and adaptability of the organic devices to the required application.<sup>[9]</sup>

The combination of organic LEDs (OLEDs) and organic photodetectors (OPDs), respectively as light-sources and light-detectors, has been recently reported in different miniaturized optical sensors such as proximity sensors,<sup>[10,11]</sup> pulse oximeters,<sup>[12–16]</sup> refractometers,<sup>[17,18]</sup> fluorescent sensors,<sup>[19–22]</sup>


M. Prosa, E. Benvenuti, M. Bolognesi, V. Ragona, S. Toffanin  
Institute of Nanostructured Materials (ISMN)  
National Research Council (CNR)  
Via P. Gobetti 101, Bologna 40121, Italy  
E-mail: mario.prosa@cnr.it; stefano.toffanin@cnr.it

D. Kallweit  
CSEM Center Muttentz  
Tramstrasse 99, Muttentz CH-4132, Switzerland

P. Pellacani, L. Lopez-Sanchez  
Plasmore s.r.l  
Viale Vittorio Emanuele II 4, Pavia 27100, Italy

M. Toerker  
Fraunhofer FEP  
Winterbergstraße 28, 01277 Dresden, Germany

F. Marabelli  
Physics Department  
University of Pavia  
Via A. Bassi 6, Pavia 27100, Italy

 The ORCID identification number(s) for the author(s) of this article can be found under <https://doi.org/10.1002/adfm.202104927>.

© 2021 The Authors. Advanced Functional Materials published by Wiley-VCH GmbH. This is an open access article under the terms of the Creative Commons Attribution License, which permits use, distribution and reproduction in any medium, provided the original work is properly cited.

DOI: 10.1002/adfm.202104927

etc.<sup>[23]</sup> In all cases, the photoresponse of the OPD is determined by the light coming from the sensing area, which is a fluorescence or a reflected-light signal triggered by the OLED emission.<sup>[24]</sup> Having a miniaturized and versatile detection scheme therefore enables the deployment of analytical devices capable to assess rapid and on-site analysis at a quality level comparable to that of laboratory tests.

At this regard, huge interest has been attracted by functionalized metallic surfaces based on surface plasmon resonance (SPR), as extremely sensitive, label-free, quantitative, versatile systems for real-time detection of single or multiple analytes.<sup>[25,26]</sup> SPR-sensors are based on surface plasmons, which are sensitive to refractive index changes. Advanced levels of sensitivity were demonstrated by the excitation of surface plasmon polaritons (SPPs). However, the need of a fine and precise control of the angle of the incident light ended up in the use of not-portable optical components in the final sensor, including laser sources and expensive prism-based optics. Although SPR-based detection scheme has become a landmark of biosensoric instruments, the need for bulky components to detect the SPR signal has prevented the use of these systems in point-of-care or in-field applications. Therefore, the lack of a miniaturized detection scheme has confined SPR instruments to laboratory-based applications. Yet, there is a timeless analytical demand on the development of a sensing system that is high performing and portable to exploit the functions of an entire lab in the field. Standard analytical techniques such as liquid chromatography, enzyme-linked immunosorbent assay (ELISA), polymerase chain reaction (PCR) are indeed designed for laboratory use only. As a result, the time and costs that are involved in the sample collection and transport to laboratories are current limitations of standard methods. With respect to standard instrumentations, a miniaturized system would also provide additional advantages, including reduced solvent consumption, cost-effectiveness, and user-friendliness. In this scenario, a very promising and alternative strategy was offered by the periodic nanostructuring of the metal surface, resulting in a nanostructured plasmonic grating (NPG),<sup>[27]</sup> in which the direct excitation of SPPs is allowed even at quasi-normal incidence, thus releasing the constrain of using high refractive index prisms.<sup>[28]</sup>

As a matter of fact, the detection scheme is a key element in building the plasmonic platform because of its contribution to the performance of the sensor. Despite individual organic devices already being used for SPR detection,<sup>[5,29]</sup> an integrated system in which an organic light-source and an organic light-detector are coupled with a plasmonic nanostructured surface has never been produced. Assembling three components with well-matched spectral characteristics is indeed not sufficient for obtaining an efficient plasmonic sensor. NPGs are angle-sensitive optical items,<sup>[30]</sup> it follows that a suitable design of the sensor layout and an accurate spatial optimization of the plasmonic and optoelectronic components need to be accomplished to make the integrated-platform effective without any additional macroscopic optical elements.

In this regard, organic light-emitting transistors (OLETs) are a fascinating class of planar optoelectronic devices in which the light emission originates from an organic field-effect transistor (OFET) structure.<sup>[31–33]</sup> The possibility to integrate a photode-

tor onto the planar OLET structure would allow to maximize the geometrical fill factor in an in-plane detection scheme. In addition to that, the intrinsic electrical switching ability of OLETs makes the sensor arranged for a possible implementation in sensor matrices without the need for a driving circuitry.

Here, we report an unprecedented ultracompact system endowed with optical and plasmonic sensing capabilities (hereafter named as optoplasmonic) through the smart integration of an OLET, an OPD and an NPG. The components and the layout of integration were suitably designed to make the three elements work cooperatively in a reflection-mode configuration. In particular, the OPD was vertically stacked onto the source electrode of the OLET thus minimizing the lateral distance between light source and light detection regions and the contact-points needed for biasing the overall system. In this regard, although multiple organic optoelectronic components have been already monolithically integrated on a single substrate or in a single device structure,<sup>[34–41]</sup> our OLET–OPD platform is the first photonic module, to our knowledge, which shows electrical switching characteristics, light-emission, and light-sensing capability in a single organic multilayer architecture. When coupled to the NPG, a multifunctional system with SPR-sensing ability was obtained at a remarkably high level of miniaturization, arising from the direct fabrication of the NPG onto the encapsulating cap of the OLET–OPD platform. The deposition of a nonconventional plasmonic nanostructure on a transparent substrate therefore allowed the optical detection from the opposite side of the grating at which the refractive index modulation occurred, thus avoiding possible issues arising from the turbidity of the liquid matrix used as a sample.

To effectively design the 3D layout of the optoplasmonic architecture, an advanced optical simulation model was suitably developed, so that the simulation considered angle- and wavelength-dependent efficiencies of all components besides their dimensions. The optimal size and relative positioning of the three elements, as well as the signal variation of the sensor under different conditions, were thus predicted. Accordingly, the effectiveness of the final miniaturized optoplasmonic system was validated by the dependence of the OPD output signal on the NPG exposure to liquid media with different refractive index, i.e., water, and ethanol solutions at different concentrations.

## 2. Results and Discussion

**Figure 1a** shows the overall layout of the optoplasmonic system. The proposed architecture consists of an OPD stacked vertically onto an OLET, whose source electrode is also the anode of the photodiode. On top of the OLET–OPD platform, which is hereafter named photonic module, an NPG is placed by its direct fabrication on the encapsulating cap. In the principle of operation of this reflective configuration, the OLET amplifies an input electrical signal to generate light, which is modulated by the NPG and it is eventually absorbed by the OPD to produce an output electrical signal. When the outer surface of the NPG is exposed to a change of refractive index ascribed to the surrounding medium, a spectral shift of the NPG reflectance

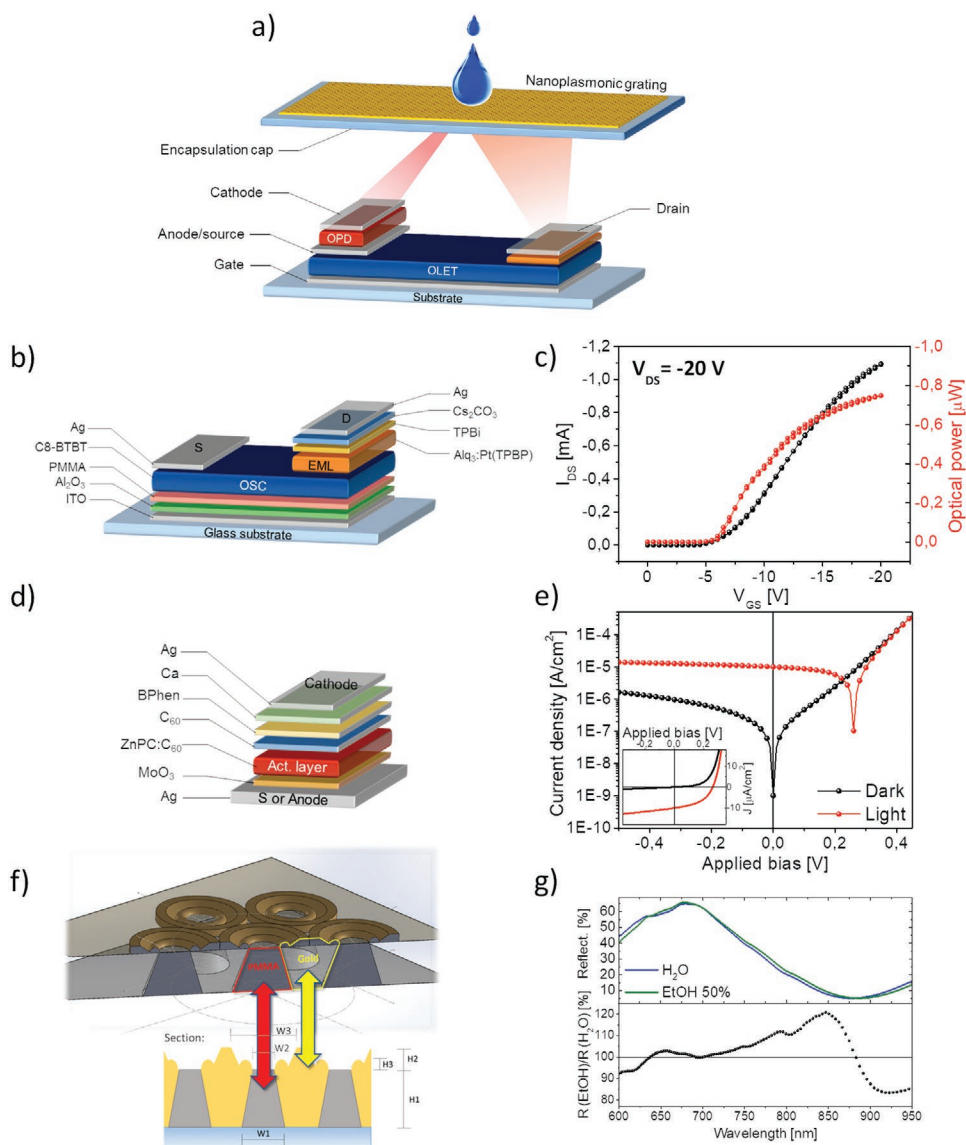


**Figure 1.** a) Simplified representation of the proposed optoplasmonic system. Schematics of the individual device subcomponents, which are b) an OLET, d) an OPD, and f) an NPG. c) OLET p-type transfer characteristics (black dots) at  $V_{DS} = -20$  V with the corresponding power of optical emission (red dots). e) OPD  $J$ - $V$  plot measured in dark conditions (black dots) and under low-light illumination (red dots), which is presented in logarithmic scale to evidence the diode-like characteristics and in linear scale (inset) to show the photovoltaic effect. g) (Top panel) Reflectance spectrum of the NPG at  $2.5^\circ$  when exposed to ultrapure water (blue line) and a 50% ethanol solution (green line) with the light impinging from the glass side. EtOH is the abbreviation for ethanol. g) (Bottom panel) Sensitivity spectrum of the NPG to a 50% of ethanol solution, calculated as the ratio of the reflectance spectra in the top panel.

occurs, and the modulation can be detected by the OPD. Likewise, if the NPG is excited with a fixed wavelength at a certain resonance angle, the intensity of the reflected light changes upon changing the NPG external surroundings. Given that in the here-proposed architecture the OLET has a defined spectrum of emission, the OPD output signal is the variable parameter to be monitored. As a result, quantitative evaluations can be easily done, once the system is calibrated, by monitoring the modulation of the magnitude of the OPD electrical signal upon changing the medium composition (so that the analyte to detect once suitable biofunctionalization of the sensing surface is performed).

It is worth mentioning that the variation of the NPG reflectance is extremely dependent on the angle of reflection and it is particularly pronounced at low angles of reflection. In this regard, the direct fabrication of the OPD onto the source electrode of the OLET provides a high proximity of the excitation and the detection regions, which are inherently separated by the length of the OLET channel (i.e., a few tens of micrometers). If considering that the NPG is directly deposited on top of the encapsulating cap of the photonic module, the implementation of the OPD onto the OLET is the key factor that allows operating at small reflection angles and that guarantees the effective operation of the proposed detection scheme at an ultracompact

size of the device. In addition to that, the proposed device-design reduces the costs of production. On one hand, the opti- less approach allows avoiding the need of expensive prisms as typically required in most SPR sensors. On the other hand, the use of deposition techniques such as colloidal lithography for the NPG and thermal sublimation for OLET and OPD, instead of the traditional and expensive laser beam lithography, drastically limits the costs of the fabrication of the optoplasmonic system.

In the development of the proposed architecture, having matched spectral properties is the basic prerequisite of the three components to interact with one another. In this regard, since most NPGs show prominent sensitivities in the near-infrared (NIR) region,<sup>[3]</sup> we developed single OLETs, OPDs, and NPGs responding at around 800 nm.

An electrophosphorescent compound based on a platinum- porphyrin complex, i.e., Pt<sup>II</sup>-tetraphenyltetrazabenzoporphyrin [Pt(tpbp)], dispersed in a matrix of tris(8-hydroxyquinoline) aluminum (Alq<sub>3</sub>) was selected as the OLET emissive layer (EML) for its strong NIR emission at around 770 nm.<sup>[42,43]</sup> As shown in Figure 1b, bottom-gate/top-contact OLETs were fabricated on a glass/indium tin oxide (ITO)/Al<sub>2</sub>O<sub>3</sub>/poly(methyl methacrylate) (PMMA) platform to ensure operating voltages compatible to real-setting applications.<sup>[44]</sup> Unipolar devices were obtained by using 2,7-dioctyl[1]benzothieno[3,2-b][1]benzo- thiophene (C8-BTBT) as a p-type charge transport material.<sup>[45]</sup> A 20 nm thick semitransparent Ag film was used as the drain electrode to permit the emission of light to the top direction in accordance with the proposed scheme of optoplasmonic detec- tion. The resulting OLETs exhibited a clear and hysteresis-free p-type behavior with a hole mobility ( $\mu_{\text{h}}$ ) of 0.16 cm<sup>2</sup> V<sup>-1</sup> s<sup>-1</sup>, current ON/OFF ratio of >10<sup>4</sup>, and a threshold voltage ( $V_{\text{TH}}$ ) as low as -6.8 V (Figure 1c; Figure S1, Supporting Information), which indicate an optimal performance of the obtained devices. In addition to that, at the drain-source voltage ( $V_{\text{DS}}$ ) of -20 V

and by sweeping the gate-source bias ( $V_{\text{GS}}$ ) up to -20 V, OLETs reported an optical emission to the top direction reaching 0.8  $\mu\text{W}$ , in great agreement with state-of-the-art values.<sup>[46,47]</sup>

The spectral characteristics of the corresponding OLETs showed an electroluminescent band at the desired peak wave- length of  $\approx 766$  nm (Figure 2). Accordingly, top-absorbing OPDs responding in the same spectral region were developed by using a photoactive layer based on a blend of zinc phthalocyanine (ZnPc) and fullerene-C<sub>60</sub> for its spectral response in the NIR region.<sup>[48]</sup> Figure 1d shows the OPD architecture in which a reflective anode and a semitransparent cathode were respectively used as the bottom and the top electrode. In a first step, 1 cm<sup>2</sup> reference devices on bare glass were prepared for device char- acterization. It is worth mentioning that, once the OPD is inte- grated into the optoplasmonic system, the OPD anode will also act as the OLET source electrode. In this view, Ag was selected as the bottom-electrode of the individual OPD. Top-absorbing OPDs showed current-voltage responses with a good diode-like behavior (Figure 1e) characterized by a low dark current den- sity <600 nA cm<sup>-2</sup> at -0.2 V and a short-circuit photogenerated current density ( $J_{\text{sc}}$ ) of 10.0  $\mu\text{A cm}^{-2}$  under low light illumination of 230  $\mu\text{W cm}^{-2}$  with AM1.5G spectrum. OPDs exhibited an external quantum efficiency (EQE) (Figure 2) of  $\approx 20\%$  in the spectral range 610–800 nm,<sup>[48–50]</sup> in great agreement with the OLET optical emission. In view of implementing the OPD into the optoplasmonic system, the linearity of the OPD response as a function of light intensity was verified with illumination at 766 nm (Figure S2, Supporting Information), i.e., the OLET peak wavelength. The linear dependence of the  $J_{\text{sc}}$  on the light inten- sity was evidenced even at an irradiance <10  $\mu\text{W cm}^{-2}$ , and the calculated responsivity value at zero bias condition was 0.1 A W<sup>-1</sup> (at 766 nm), in great agreement with the responsivity values of OPDs typically used in optical sensors.<sup>[14]</sup>

According to the spectral characteristics of the OLET and the OPD, an NPG sensitive to refractive index modulations

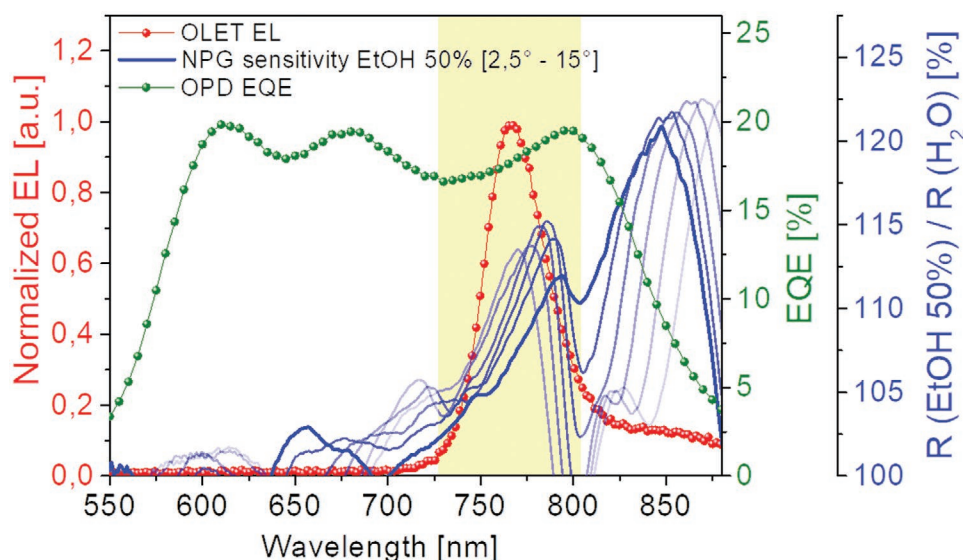


**Figure 2.** Normalized electroluminescence (EL) spectrum of OLETs (red dots), EQE spectrum of the OPDs (green dots), and sensitivity spectra of the NPG (blue lines) to a 50% ethanol solution. The different spectra of the NPG sensitivity refer to angles of reflection ranging from 2.5° (blue line) to 15° (light blue line). For clarity, only the positive region of the spectra of sensitivity is shown. Complete spectra are reported in Figure S4 in the Supporting Information. The yellow area highlights the main spectral region of overlap of the response of individual components.

was fabricated on a transparent substrate. In view of its implementation in the optoplasmonic architecture, a typical encapsulating glass was used as a substrate, that is indeed the key factor to enable the operation of the final optoplasmonic system.

The NPG consisted of a hexagonal lattice of PMMA truncated cones (pillars) embedded in an optically thick Au layer, with a small Au ring surrounding the top of each PMMA pillar (Figure 1f; Figure S3, Supporting Information). In the NPG development, suitable grating pitch, i.e., the center-to-center distance between two PMMA pillars, and pillar size were adopted to tune the optical response and optimize the surface sensitivity at 766 nm. To analyze the reflectance characteristics of the NPG, the light was shone through the glass side at quasi-normal incidence. When exposing the NPG surface to ultrapure water, the reflectance spectrum exhibited a broad plasmonic resonance around 850–900 nm (Figure 1g), and the reflectance was >30% at 766 nm. A modulation of the reflectance spectrum was evidenced when a solution of 50% (v/v) of ethanol/water was used instead of the ultrapure water. The use of an ethanol solution as a medium of interest is ascribed to the simple and fast modality to obtain a refractive index change by considering that of pure water as the reference. In particular, the index change correlated to the transition from pure water to an ethanol concentration of 50% is as low as  $2.5 \times 10^{-2}$  RIU (i.e., 25000 RU),<sup>[51]</sup> which roughly corresponds to the SPR signal generated in commercial instruments by 10 ng mm<sup>-2</sup> of proteinous material at the sensor surface.<sup>[30]</sup>

The sensitivity of the NPG, defined as the ratio between the two reflectance spectra, showed positive values in the range 637–882 nm. While the maximum sensitivity was peaked at 847 nm, a second band centered at 792 nm exhibited values over 106% in the proximity of the OLET maximum peak of electroluminescence (Figure 1g). However, the angular dependence of the sensitivity of the NPG must be also considered. Indeed, according to the geometrical positioning of the subcomponents in the optoplasmonic system, the operational range of reflection angles is defined by i) the lateral distance between the coplanar light-source and light-detection regions of the photonic module, ii) the width of the OPD, and iii) the vertical distance between the plane of the light source/detection and the NPG surface, which roughly corresponds to the thickness of the encapsulating glass. From a simplistic ray-optics evaluation based on the geometrical characteristics of individual components, the NPG in the optoplasmonic system would operate in the angular reflection range of about 4°–63° when assuming an OLET–OPD lateral distance of 70 μm (i.e., the OLET channel length), an OPD width of 500 μm (i.e., the typical width of an OLET source electrode), and a thickness of the encapsulating cap of 1.1 mm.

In this regard, by increasing the angle in the reflectance measurements of the NPG toward the range of operation expected in the optoplasmonic system, an increase of the sensitivity at the OLET peak wavelength of 766 nm was observed (Figure 2; Figure S4, Supporting Information). Therefore, a perfect superposition of the NPG sensitivity with the OLET emission is evidenced (Figure 2). As a final and mandatory check, we observe that the spectral region of overlap between the OLET emission and the NPG sensitivity is fully covered by the EQE spectrum of the OPD. It follows that the three independent optoelectronic and plasmonic components are suitably

designed to optically interact when integrated in a single functional system.

However, the above-described assumptions do not consider other additional intrinsic factors of the optoplasmonic system such as i) the OLET has a large emission area and thus cannot be considered as a point-like source, ii) the OLET emission is not collimated, rather it is wide-angle (Lambertian),<sup>[46]</sup> and iii) the NPG is a 3D structure that is extremely sensitive to the wavelength of excitation, local changes of refractive indexes, and small changes of the incident angle of optical excitation in both *x* and *y* directions, defined as the planar coordinates of the photonic module.

A simulation model was therefore developed to design the most effective layout of the system with the aim of unravelling the full potential of the detection scheme. The model included the metrics and the structural characteristics of each individual component in order to i) identify the most sensitive area of the photonic module and ii) determine the best positions, sizes, and reciprocal distances of the optoplasmonic components.

This was achieved by splitting the simulation in two parts: i) the rigorous optical simulation of the NPG, and ii) the optical simulation of the complete optoplasmonic system based on a much faster field tracing approach that, in contrast to ray tracing, also considers diffraction, interference (phase), and polarization.

Regarding the NPG, because of its metallic nature, many evanescent diffraction orders ought to be considered in the rigorous simulation to achieve a suitable degree of accuracy. Considering the number of wavelengths of the OLET emission, the 3D structure of the NPG would lead to tremendous calculation efforts. Therefore, the NPG was modeled as a “programmable mirror” component, where its angular spectral reflection efficiencies for discrete incidence angles were stored in a precalculated lookup table. Lookup tables were automatically interpolated from discrete data collected on real samples. They comprised reflection efficiencies, wavelengths, and the influence of different media at the surface of the NPG. An experimental characterization of the angular-dependent (between 2.5° and 62.5°) and polarization-dependent (transverse electric and transverse magnetic) reflectance was, therefore, previously performed (Figure S4, Supporting Information). Regarding the OLET, the model considered the influence of the large emission area, the wide angle (Lambertian) emission, and the power spectrum of the OLET to simulate the angular spectral irradiance impinging the NPG. Since the emission of the here-described OLET involves only the inner edge of the drain electrode,<sup>[45]</sup> the simulated lateral (*x*) dimension of the emissive area was limited to 100 μm of the total width of the drain electrode. The total length of 11.94 mm was instead considered in the transversal (*y*) dimension.

Upon this preliminary activity, the light intensity distribution in the plane of the photonic module was simulated. Spectrally weighted fields were traced to the NPG and, based on the spectral angular dependent reflection efficiencies, the light was reflected back onto the plane of the photonic module. When the NPG is covered with ultrapure water, the light distribution is almost homogenous in the region around the OLET (Figure 3a), which extends a few millimeters along the lateral *x*-dimension.

The simulation was repeated for the NPG being covered by a 50% ethanol solution, and the relative change of the light

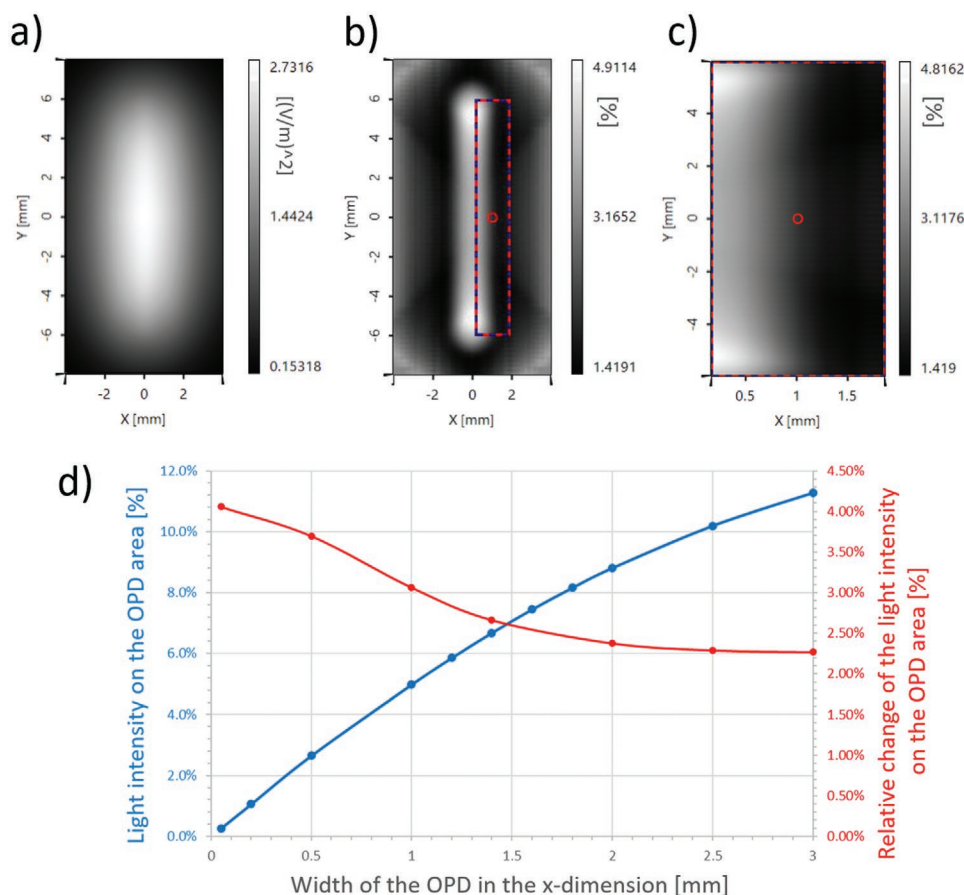


**Figure 3.** a) Top-view simulation of the light intensity distribution in the OLET–OPD plane when exposing the NPG to ultrapure water. b) Simulation of the relative change of the light intensity distribution in the OLET–OPD plane when the NPG undergoes a transition from exposure to pure water to a 50% ethanol solution. The dotted rectangular area highlights the relative change on the OPD area, which has a size of 1.7 mm  $\times$  11.94 mm. Panel (c) shows the magnification of that area, in which the integral results to be 2.5%. All images are top-view representations, in which the OLET is placed at  $x = 0$ . d) (Blue line) Dependence of the percentage of the OLET light reaching the OPD area on the lateral dimension of the OPD when the NPG is exposed to a 50% ethanol solution. d) (Red line) Relative change of the light intensity on the OPD area as a function of the lateral dimension of the OPD, when passing from the NPG exposed to pure water to a 50% ethanol solution.

distribution that is involved in the transition from ultrapure water to a 50% ethanol solution was analyzed. As indicated by brighter areas in Figure 3b, the highest relative change was obtained as close as possible to the light source. Hence, the closer the OPD is to the OLET, the higher the sensitivity of the system is. In this regard, the developed simulation model also has the capability to predict the system's sensitivity in a specific area in which the OPD is placed, as highlighted by the dotted rectangle in Figure 3b. Thus, the best position and size of the OPD in the plane of the OLET can be found. For this analysis, a minimum OLET–OPD lateral distance of 170  $\mu\text{m}$  was introduced in the calculation to ensure the OLET channel length (i.e., 70  $\mu\text{m}$ ), and fabrication tolerances (i.e.,  $\approx 100 \mu\text{m}$ ). In addition to that, the size of the OPD in the in-plane transversal ( $y$ ) direction was limited to the substrate size, i.e., a maximum of 11.94 mm. Hence, the size of the OPD was only varied in lateral ( $x$ ) direction.

As shown in Figure 3d, the relative change of the light intensity is maximized for small widths of the OPD in the lateral ( $x$ ) direction. However, reducing the  $x$ -dimension of the OPD would also lead to a reduction of the overall amount

of light which could be collected, thus leading to smaller photocurrents.

To favor the signal collection, the best trade-off between the intensity of the reference signal, recorded when the optoplasmonic system is exposed to water, and the magnitude of the relative signal change was found at the OPD horizontal dimension of 1.7 mm. According to the proposed layout, the simulation of the total percentage of signal variation with respect to the reference signal amounted to 2.5% (Figure 3c,d). This means that the intensity of the reference signal is eventually modified of about 2.5% by the medium of interest, which is in this case a solution of 50% of ethanol.

Figure 4a shows a picture of the chip fabricated by following the simulated layout. Multiple photonic modules, i.e., 7 OLETs alternated to 8 OPDs, were placed on a single substrate to generate an interdigitated architecture with a linear geometry. In view of developing a sensor capable to detect multiple analytes, this type of striped geometry can be easily connected to the channels of a microfluidic module.

The OPD was fabricated on an Ag layer with the dual functionality of being both the source electrode of the OLET and the

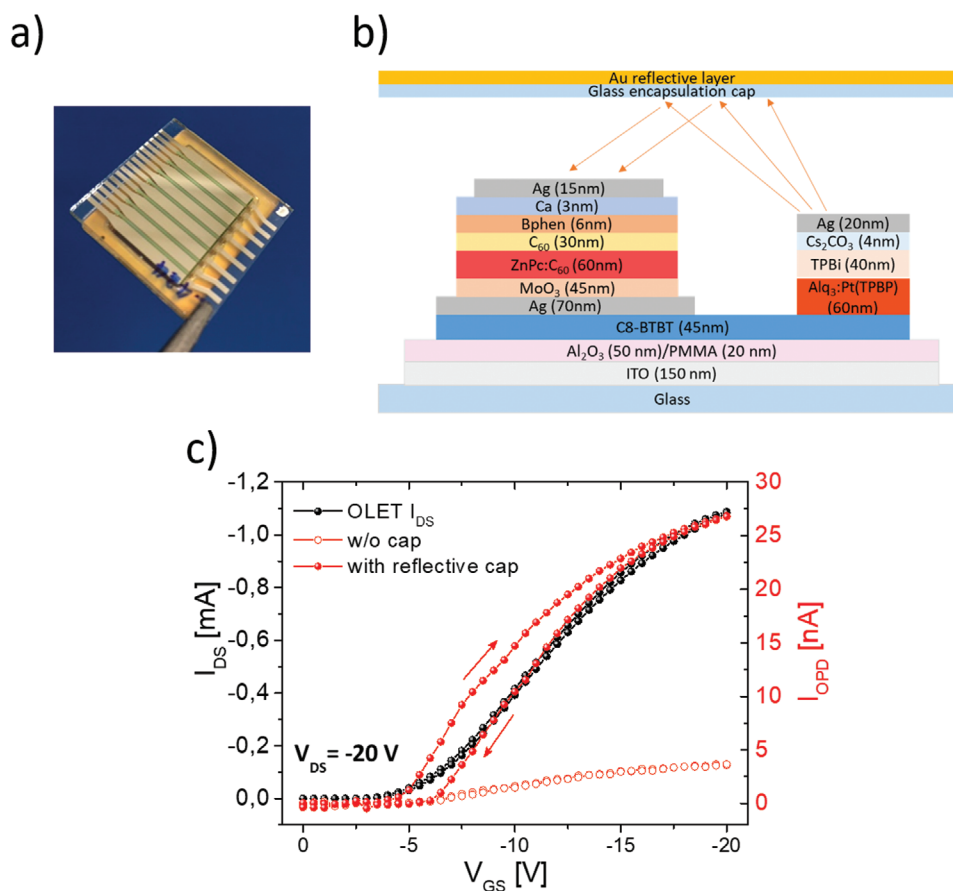


**Figure 4.** a) Picture of the bottom side of the photonic module. b) Schematics of the cross-section of the photonic module including an Au-covered cap to reflect the OLET light to the adjacent OPD. c) Transfer p-type characteristics of the OLET (black dots) measured at  $V_{DS} = -20$  V, and the corresponding current photogenerated by the adjacent OPD (red dots) in the photonic module respectively without (empty dots) and with (filled dots) the use of a reflective cap. Since the OLET  $I_{DS}$  is measured in a double scan mode (forward and backward) as a function of  $V_{GS}$ , two red arrows indicate the correlated OPD photocurrent.

anode of the OPD (Figure 4b). Despite the surface characteristics of the anode had changed with respect to the independent component, the OPD current–voltage response still showed a good diode-like behavior (Figure S5a, Supporting Information), and an EQE with unchanged spectral features and values over 10% at the OLET emission wavelength of 766 nm (Figure S5b, Supporting Information). The fabricated optoplasmonic system exhibited the desired structural characteristics as shown by optical microscopic images (Figure S6, Supporting Information), where the OLET channel length was 70  $\mu\text{m}$  and small lateral displacements ensured an efficient stacking of the OPD layers. A pyramidal disposition of the organic layers was used to avoid possible short-circuits between the bottom source/anode and the top cathode electrodes, as already indicated in the simulation method.

As a preliminary check of the single components' operation, the photonic module, i.e., the OLET–OPD platform, was first characterized without encapsulating glass. In this architecture, the light-emitting region is mainly located at the inner edge of the OLET drain electrode (Figure 4b; Figure S8c, Supporting Information), according to the intrinsic micrometer-sized emission capability of the OLET structure.<sup>[45]</sup> The generated light is directed to the top-side and it is not expected to reach the OPD.

The same measure was repeated after the encapsulation of the photonic module with a cap being covered by a reflective Au coating to direct the light to the OPD (Figure 4b). In the protocol of operation, the OPD was driven in short-circuit conditions in order to maximize its sensitivity, while the OLET was driven at a constant  $V_{DS}$  of  $-20$  V by sweeping the bias between the gate (i.e., ITO) and the source from 0 to  $-20$  V in order to maximize the optical emission power.

As shown in Figure 4c, the OLET of the photonic module exhibited a similar electrical behavior as that of the independent device (Figure 1c), with a clear and hysteresis-free p-type transfer curve characterized by a  $\mu_{th}$  of  $0.14 \text{ cm}^2 \text{ V}^{-1} \text{ s}^{-1}$  and a  $V_{TH}$  of  $-5.4$  V. During this OLET characterization, the OPD photocurrent was continuously collected. In the case of the photonic module without encapsulating glass, a slight increase of the current photogenerated by the OPD as a function of the OLET  $V_{GS}$  was observed despite the fact that the optical emission was not supposed to reach the OPD (Figure 4c). It is likely that the OPD was reached by stray light from the OLET given the lateral proximity between the two components. However, when using a reflective encapsulation onto the photonic module, the OPD photocurrent as a function of the OLET  $V_{GS}$  showed a drastic increase reaching values close to 30 nA (Figure 4c). If compared

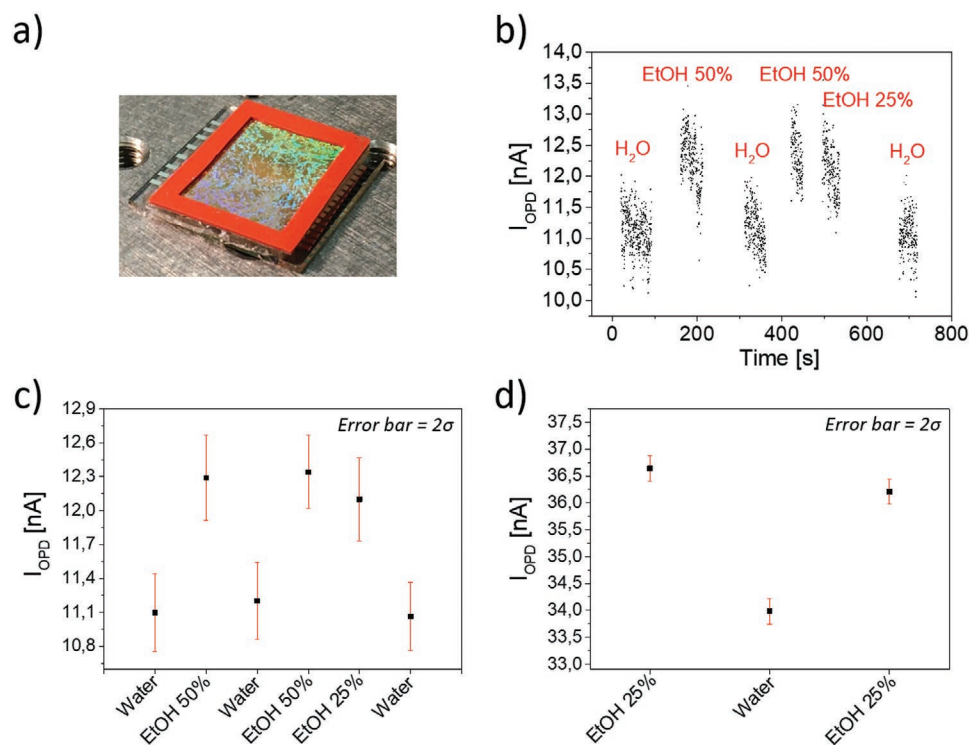


**Figure 5.** a) Picture of the top-side of the optoplasmonic system covered by a silicon sheet to contain the liquid onto the NPG. b) Photocurrent generated over time by the OPD within the optoplasmonic system, when the NPG is exposed to ultrapure water and 25% and 50% ethanol solutions. c) Mean photocurrent of the OPD of the optoplasmonic system with the relative standard deviation when the NPG is exposed to ultrapure water and 25% and 50% ethanol solutions. d) Mean photocurrent of two adjacent OPDs of the interdigitated optoplasmonic system, with the relative standard deviation, when the NPG is exposed to ultrapure water and a 25% ethanol solution.

to the reflection-less architecture, a sevenfold increase of the OPD photocurrent was evidenced by using the Au coating. The same finding was also observed from other different driving modes of the photonic module (Figure S7, Supporting Information), thus confirming the effective operation of the proposed reflection-mode architecture. Furthermore, if using the interdigitated chip in which two OPDs collect the light generated by the OLET between them, the photogenerated current was doubled (Figure S8, Supporting Information) thus increasing the capability to collect optical signals.

Eventually, the use of the NPG-covered glass as the encapsulation of the photonic module led to the smart-integrated sensor (Figure 5), at a remarkable size of  $0.1 \text{ cm}^3$  per optoplasmonic system. An adhesive silicon sheet was placed onto the outer surface of the NPG serving as the container of the liquid, in conjunction with a thin cover glass, to avoid the percolation of the medium and its evaporation during the measurements. By keeping the OLET in the ON state at  $V_{DS} = V_{GS} = -20 \text{ V}$ , ultrapure water and a 50% ethanol solution were flowed alternatively over time onto the NPG surface, while the OPD photocurrent was simultaneously measured at zero bias. In order to increase the accuracy of the test, the OPD photocurrent was measured every 50 ms for at least 50 s for each liquid medium. The use of a transparent glass/ITO/ $\text{Al}_2\text{O}_3$ /PMMA platform allowed monitoring possible undesired effects influencing the measurement, such as the reduction of the OLET optical emission over time (Figure S9, Supporting Information). An external photodiode was indeed placed at the bottom side of the

system to collect the bottom-emitted light over the entire duration of the test. In addition to that, the photoresponse of the OPD over time was preliminary analyzed to ascertain that the OPD characteristics were stable for the entire duration of the test (Figure S10, Supporting Information).

It is worth reminding that in the principle of operation of the optoplasmonic chip, the OLET light impinges the transparent backside of the NPG, and it is modulated upon changing the surroundings at the NPG outermost surface. Since the OLET light is reflected back to the OPD, which converts it into an output electrical signal, the alternation of a liquid of analysis onto the NPG with respect to the reference liquid induces a variation of intensity of the reflected light and hence a modification of the OPD photocurrent.

When exposed to ultrapure water, an OPD photocurrent of  $11.1 \pm 0.3 \text{ nA}$  was measured from the optoplasmonic system (Figure 5b). If compared to the magnitude of the OPD photocurrent recorded on the purely reflective-mode architecture at the same driving conditions (Figure 4c), a threefold reduction can be observed, which is the consequence of the NPG reflectance of  $\approx 30\%$  at  $766 \text{ nm}$  with respect to a full-reflective coating. Notably, a clear increase of the OPD photocurrent from  $11.1 \pm 0.3 \text{ nA}$  to  $12.3 \pm 0.3 \text{ nA}$  was evidenced when exposing the NPG surface to a 50% ethanol solution (Figure 5c). The optoplasmonic system resulted to be sensitive to the proposed medium.

In this regard, quantitative analyses were carried out by testing the optoplasmonic system with a 25% ethanol solution.



As shown in Figure 5b,c, a clear increase of the OPD photocurrent was recorded when passing from ultrapure water to 25% of ethanol. Nevertheless, the error bars associated to these results do not allow an accurate evaluation. In order to improve the signal-to-noise ratio, the interdigitated chip was exploited to increase the absolute photocurrent values by collecting the photocurrent generated by both OPDs adjacent to the OLET. Best results are shown in Figure 5d, in which a clear signal variation due to the presence of a 25% ethanol solution was eventually detected.

From experimental data, we calculated the relative signal variation ( $\Delta I/I_0$ ), which is the ratio between i) the signal difference when passing from pure water to an ethanol solution ( $\Delta I$ ) and ii) the OPD photocurrent when the NPG is exposed to pure water ( $I_0$ ). More specifically,  $\Delta I/I_0$  of the optoplasmonic system amounted to 7% and 11% when the medium on the NPG surface is changed from water to 25% and 50% of ethanol solutions, respectively. The dependence of  $\Delta I/I_0$  on the analyte concentration is in agreement with simulated results (Figure 3; Figure S11, Supporting Information), which predicted a signal variation of 1.5% and 2.5% for 25% and 50% of ethanol, respectively. Despite a slight mismatch between experimental and calculated  $\Delta I/I_0$  values being evidenced, the ratio between theoretical and experimental values is preserved regardless the different solution concentrations. Indeed, both simulations and experimental data showed a  $\Delta I/I_0$  that almost doubled when passing from 25% to 50% of ethanol: from 1.5% to 2.5% in the simulated case, and from 7% to 11% in the experimental one. The mismatch highlights possible systematic factors not considered in the description of the complex architecture of the smart-integrated system, such as tilted NPG with respect to the photonic module, possible variations of the encapsulating cap thickness, etc.

If our results are overlapped to the calibration curve for alcoholic solutions of a commercial nanoplasmonic instrument,<sup>[28]</sup> which are both based on a similar NPG surface, it can be found a good match with the typical linear trend of  $\Delta I/I_0$  as a function of refractive index variation ( $\Delta n$ ) in a double logarithmic scale (Figure S12, Supporting Information). The comparison evidences the good level of accuracy of our results with respect to commercial instruments and it thus confirms the potential of the here-proposed organic ultracompact system for plasmonic-based detection.

Although the commercial instrument is capable to detect a  $\Delta n$  as low as 4 RU, while the  $\Delta n$  measured by our optoplasmonic system amounted to 14 000 RU (transition water  $\rightarrow$  25% ethanol solution), the possibility to further optimize the figures of merit of each of the three optoplasmonic subcomponents (such as the optical power emitted by the OLET) would further improve the sensitivity of the system. In addition to that, the use of advanced ambipolar OLETs able to span the light stripe horizontally in the channel would also favor the optical pig-tailing and thus maximize the plasmonic signal.<sup>[8]</sup>

Despite the use of collimated light sources or, for instance, additional optical elements to tune the optical signal could be an alternative approach to boost the sensitivity of the system, the limitations in terms of cost and miniaturization of those components would outrun the benefits of enhancing the sensitivity. The here-proposed optoplasmonic system that is based

on the combination of a smart design of the layout and the use of a planar OLET platform opens to an advanced level of miniaturization of the sensor, which indeed had a total size as low as 0.1 cm<sup>3</sup>. Moreover, the use of versatile and low-cost organic optoelectronic components operating at low-bias conditions and nanoplasmonic surface prone to easy biofunctionalization represents a step forward toward the achievement of cost-effective multiplexing and quantitative sensing systems to be used in the daily life.<sup>[28]</sup>

### 3. Conclusion

An ultracompact device with sensing capability was demonstrated through the smart integration of versatile and low-cost optoelectronic and plasmonic components. The direct integration of the OPD onto the in-plane structure of the OLET provided unprecedented proximity of the microscaled light-source and the light-detection area, which enabled the exploitation of the angle-dependent sensing characteristics of the NPG.

Based on experimental data, an advanced simulation tool was developed to design the most effective layout of integration and to predict the signal variation at the NPG sensing surface under different external conditions. Accordingly, the fabricated optoplasmonic system exhibited the remarkable capability to recognize the presence of a 50% of ethanol solution, with respect to pure water, at an ultracompact sensor size of 0.1 cm<sup>3</sup>. Through the development of an interdigitated architecture, the optoplasmonic system was able to perform quantitative analyses, thus signal modulations were clearly recorded even when reducing the ethanol concentration from 50% to 25%.

Despite the relatively low brightness of OLETs, which is correlated to the underdevelopment of the technology, the good match of our results with the calibration curve of commercial instruments using a similar NPG highlights the potential of the here-reported approach.

The optimization of the optical response of all three sub-components of the optoplasmonic system would additionally contribute to increase the level of detectivity, as shown by the interdigitated chip and indicated by simulations. In addition to that, further developments on the intrinsic OLET characteristics would drastically boost the sensitivity of the optoplasmonic system. For instance, ambipolar OLETs are capable to spatially control the micrometer region of emission, upon changing the bias applied to the device, toward a fine optimization of the angular operation of the NPG. In particular, the light stripe can be moved along the micrometric-long channel of the OLET in the direction toward the OPD area to further reduce the angles of operation in the detection scheme. Hence, ambipolar OLETs would provide the sensor of the pivotal possibility to maximize the sensitivity upon changing the operational applied-bias conditions. Diversely, the possible use of well-assessed light-emitting technologies, such as OLEDs, as replacement to OLETs would drastically increase the complexity and the cost of the system as a result of the high level of accuracy that would be required in the monolithic fabrication of the OLED and the OPD to fulfill a quasi-normal detection. In a system in which an OLED–OPD lateral distance of a few micrometers must be guaranteed, advanced fabrication equipment and extremely

accurate fine metal masks would be therefore necessary for the thermal deposition of all layers of both devices.

The here proposed optoplasmonic system therefore represents a first step toward an application-driven use of the OLET technology for the realization of a new class of ultracompact and highly sensitive sensors in which the plasmonic signal can be maximized by playing on the operational optoelectronic parameters.

## 4. Experimental Section

**Simulation:** A simulation tool for the analysis of the 3D light pathways was developed. The optical simulation comprised two main parts: i) the possibility to rigorously analyze the NPG by means of the Fourier model method (FMM, also called rigorous coupled wave analysis (RCWA)); ii) the simulation of the complete optoplasmonic system via tracing fields, which allows considering polarization, diffraction, and interference, and representing the NPG by a “programmable mirror,” which describes the angular and spectral reflection response of the NPG via lookup tables.

The FMM allows to rigorously calculate the reflection efficiencies for incoming plane waves with different wavelengths, polarizations, and angles of incidence. The core of the FMM is a 3D model of the subwavelength plasmonic grating (which does not necessarily need to be a plasmonic grating, but also any other kind of grating; e.g., a resonant waveguide grating). This model includes the nanostructure of the grating (e.g., period, shape, height) as well as the different materials and their optical properties (e.g., refractive index, absorption coefficient, layer thicknesses), which is then discretized in  $x$  and  $y$  directions. Since the here-reported grating was variant in all three dimensions, a 3D model and simulation was made. Since the FMM in its basic form assumes periodical structures that ideally extend until infinity, a unit cell of the grating was designed which then, by the simulation algorithm, was periodically replicated in  $x$  and  $y$  directions.

The complete system was then modeled with three main components: 1) OLET (Lambertian light source), 2) the grating being illuminated by the OLET and reflecting the light, and 3) the OPD that detects a certain portion of that light. The grating underwent a complete RCWA/FMM. Alternatively, the angular spectral reflection efficiencies can also be derived from lab measurements. This analysis returns a lookup table, which shows what percentage of light is returned for a given wavelength, polarization, and incidence angle in  $x$  and  $y$  directions. These values were loaded into a programmable “mirror” component, which then allows to analyze the incoming light wave and to locally determine the angle of incidence, which means their angular components alpha and beta (i.e.,  $\alpha$  and  $\beta$  angles indicating the inclinations toward the  $x$  and the  $y$  axes). Upon incidence of light emitted by the OLET, the special “mirror” component calculates the local incidence angles of the light wave and reflects the light at a percentage given by the afore-stored lookup table (derived by means of rigorous calculation via RCWA/FMM or lab measurements).

**Device Fabrication—OLET:** A transparent glass/ITO substrate (dimensions: 25 mm  $\times$  25 mm) was used for the OLET fabrication. The ITO surface was successively covered by a  $\text{Al}_2\text{O}_3$  layer (thickness: 50 nm) and a PMMA buffer layer (Allresist; thickness: 20 nm), which were respectively deposited by atomic layer deposition and spin coating. On the dielectric surface, the organic active region comprised a stacked multilayer of i) a 45 nm thick layer of C8-BTBT (Sigma-Aldrich, sublimated grade,  $\geq 99\%$ ) as a p-type semiconductor, ii) a 60 nm thick host-guest emissive layer composed by  $\text{Alq}_3$  (Sigma-Aldrich sublimated grade, 99.995%) and Pt(TPBP) (Lumtec), respectively, used as host and guest components (doping percentage: 6%), iii) a 40 nm thick layer of 2,2',2''-(1,3,5-benzinetriyl)-tris(1-phenyl-1-*H*-benzimidazole) (TPBi, Sigma Aldrich), and iv) a 4 nm thick layer of  $\text{Cs}_2\text{CO}_3$  (Sigma Aldrich, 99%). TPBi and  $\text{Cs}_2\text{CO}_3$  were used as electron injecting layers. According to

state-of-the-art OLETs,<sup>[52]</sup> nonplanar source (70 nm) and drain (20 nm) electrodes were deposited in direct contact of the C8-BTBT and onto the stacked multilayer, respectively. Organic layers and electrodes were deposited by thermal evaporation in a high-vacuum deposition chamber at a base pressure of  $10^{-8}$  mbar using shadow masks.

OLETs were fabricated with the following geometrical characteristics: channel width ( $W$ ) of 12 mm, channel length ( $L$ ) of 70  $\mu\text{m}$ , and source/drain electrode width of 500  $\mu\text{m}$ .

All chemicals were used as received without further purification.

**Device Fabrication—OPD:** The deposition of the organic and metal layers of the OPD was carried out by vacuum thermal evaporation in a high-vacuum deposition chamber at a base pressure of  $10^{-8}$  mbar.  $1\text{ cm}^2$  top-absorbing OPDs were fabricated onto a glass substrate by using a thin semitransparent Ag layer and a thick reflective Ag layer as top and bottom electrodes, respectively. The OPD multilayer structure was: glass/Ag (thickness: 70 nm)/ $\text{MoO}_3$  (thickness: 45 nm)/ZnPc:fullerene- $\text{C}_{60}$  (mixing ratio: 50:50; total thickness: 60 nm)/fullerene- $\text{C}_{60}$  (thickness: 30 nm)/bathophenanthroline (Bphen, thickness: 6 nm)/Ca (thickness: 3 nm)/Ag (thickness: 15 nm).

ZnPc and  $\text{C}_{60}$  were purchased by Sigma-Aldrich and they were sublimed twice by CreaPhys (Dresden, Germany) before utilization. All other chemicals were used as received without further purification.

The same structure was then transferred to the integrated device by depositing the organic stack and the semitransparent cathode onto the Ag source electrode of the OLET.

**Device Fabrication—NPG:** The fabrication of the NPG refers to a multistep method based on a combination of colloidal lithography and plasma processes. Glass caps were used as substrates. After a deep solvent cleaning, the cap surface was activated by an  $\text{O}_2$  plasma to promote the adhesion of a PMMA (Microresist Technology) layer, deposited by spin coating with a controlled thickness. Then, an ordered 2D monolayer of polystyrene beads was transferred on top of the PMMA layer within a Langmuir-Blodgett trough (KSV Instruments Ltd.), acting as sacrificial mask for the following etching step. Indeed, the crystalline monolayer was conditioned by a reactive  $\text{O}_2$  plasma etching, leading to a decrease of the bead diameter and consequently a pillar-like structure on the underlying polymeric layer. Thus, a layer of gold was deposited by magnetron sputtering to fill the areas exposed after the plasma etching. The residuals of colloidal mask were then removed by bath ultrasonication in a proper solvent. As a final step, an annealing treatment at 300  $^\circ\text{C}$  was performed to give more stability to the gold layer and to contribute to a better definition of the surface motives around the pillar top.

The resulting NPG consisted of a hexagonal lattice of PMMA pillars embedded in an optically thick gold layer. The process conditioning parameters were optimized in order to obtain a main plasmonic resonance and, consequently, a surface sensitive region around 770 nm. The selected grating period was 500 nm and the thickness of both PMMA and gold layer was nominally 150 nm. According to Figure 1f, the dimensions of the NPG features were: width 1 ( $W1$ ) = 300 nm,  $W2$  = 275 nm, height 1 ( $H1$ ) = 150 nm,  $H2$  = 35 nm, and  $H3$  = 15 nm.

**Device Fabrication—Photonic Module and Optoplasmonic System:** OLETs and OPDs composing the photonic module were fabricated on a transparent glass substrate by thermal deposition in a high-vacuum deposition chamber at a base pressure of  $10^{-8}$  mbar. The NPG was deposited onto the external surface of an encapsulating glassy cap. The optoplasmonic system was then obtained by sealing the photonic module with the decorated cap. The transparent substrate of the device (25 mm  $\times$  25 mm) was covered by a patterned ITO layer serving as: i) the OLET gate electrode and ii) the external electrical connection of all OLET and OPD electrodes. On a single substrate, an alternated series of source and drain electrodes was deposited to compose the interdigitated OLET architecture. The OLET channel length was 70  $\mu\text{m}$ . Overall, eight linear source electrodes and seven linear drain electrodes were deposited onto a single substrate. Onto each source electrode, an OPD was fabricated. More specifically, OLETs and OPDs had the following geometrical characteristics: 11.94 mm of length in the  $y$ -direction, 70  $\mu\text{m}$  of lateral distance in the  $x$ -direction between OLET and OPD (i.e., the

OLET channel length,  $L$ ), 1.9 mm of width ( $x$ -direction) of the source electrode/anode, 1.7 mm of width ( $x$ -direction) of the OPD cathode, and 500  $\mu\text{m}$  of width ( $x$ -direction) of the drain electrode. All the fabricated devices showed a reproducible source–drain distance of  $70 \pm 10 \mu\text{m}$  and a perfect alignment with the ITO pattern. OPDs were fabricated onto the OLET source electrode and a pyramidal stack of layers was used to avoid short-circuits between the anode/source and the cathode.

In the fabrication of reflective-like devices, photonic modules were encapsulated with caps covered on their external surface by an 80 nm thick gold layer. A UV-cured glue (UV-Resin XNR5516Z-B1, Nagase) was used for the encapsulation.

A press-to-seal silicon sheet (Invitrogen) was used in conjunction with a glass cover slip to contain the liquid onto the NPG during the optoplasmonic tests.

**Device Characterization—OLET:** Standard electrical measurements were performed in a glovebox using a standard SUSS probe station coupled to a B1500A Agilent semiconductor device analyzer. The optical output was measured either from the top and from the bottom side (i.e., through glass/ITO) of the OLET by using silicon photodiodes (sensitivity of  $0.49 \text{ A W}^{-1}$  at 766 nm) directly in contact or as close as possible to the device to collect all photons. The field-effect hole mobility and threshold gate voltage were estimated from the transfer curves in the linear regime,<sup>[53]</sup> at  $V_{\text{DS}} \ll (V_{\text{GS}} - V_{\text{TH}})$  with a grounded source electrode, using the equation  $I_{\text{DS}} = (W/L) \cdot C_i \cdot \mu_{\text{lin}} \cdot [(V_{\text{GS}} - V_{\text{TH}}) \cdot V_{\text{DS}}]$ , where  $I_{\text{DS}}$  is the measured source–drain current,  $W$  is the channel width,  $L$  is the channel length,  $\mu_{\text{lin}}$  is the field-effect mobility in the linear regime,  $C_i$  is the capacitance of the dielectric,  $V_{\text{GS}}$  is the gate voltage,  $V_{\text{DS}}$  is the drain voltage, and  $V_{\text{TH}}$  is the threshold voltage. The total capacitance of the  $\text{Al}_2\text{O}_3/\text{PMMA}$  dielectric bilayer was estimated by considering the series connection of theoretical capacitances and the individual thickness of the two layers. In particular, the overall capacitance ( $C_{\text{TOT}}$ ) of the bilayer dielectric was estimated to be  $8.38 \times 10^{-8} \text{ Far cm}^{-2}$ , as a result of the following calculation:  $C_{\text{TOT}}^{-1} = C_{\text{PMMA}}^{-1} + C_{\text{Al}_2\text{O}_3}^{-1}$ , where the capacitance of a 20 nm thick layer of PMMA ( $C_{\text{PMMA}}$ ) amounted to  $1.59 \times 10^{-7} \text{ Far cm}^{-2}$ , and the capacitance of a 50 nm thick layer of  $\text{Al}_2\text{O}_3$  ( $C_{\text{Al}_2\text{O}_3}$ ) amounted to  $1.77 \times 10^{-7} \text{ Far cm}^{-2}$ .

Electroluminescence spectra on encapsulated OLETs were measured in air by using a calibrated optical multichannel analyzer (PMA-11, Hamamatsu).

**Device Characterization—OPD:** OPDs were characterized in dark conditions inside a glovebox using a standard SUSS probe station coupled to a B1500A Agilent semiconductor device analyzer. The same equipment was also used while illuminating the device under a AM1.5G simulated solar irradiation (Abet Technologies Sun 2000 Solar Simulator). Tests under low-light illumination were performed with a commercial LED (OSA Opto Light) emitting in the range 760–780 nm. EQE measurements were performed using an optical setup based on following components: ASBN-W100 tungsten-halogen light source, Digikröm CM110 1/8m monochromator (Spectral Products), Chopper MC2000 (THORLABS Inc.), lock-in amplifier 7270 (AMETEK Inc.), and current preamplifier 5182 (AMETEK Inc.). A Standard Photodiode Power Sensor S120VC (THORLABS Inc.) was used for calibration of the system. Measurements were carried out at zero device BIAS and chopper frequency 83 Hz.

The OPD photocurrent stability was measured at 0 V over a period of 1000 s. The OPD was illuminated with an inorganic NIR-LED (LED770 from THORLABS, center wavelength 770 nm) after 10 min of LED warm up.

**Device Characterization—NPG:** Scanning electron microscopy (SEM) images of the nanostructured plasmonic gratings were acquired by using the Nova 600i Dual Beam (FEI) to evaluate the morphological characteristics of the surface motives.

A preliminary optical characterization of the surface optical response in air and in different media with defined refractive indexes was carried out with an inverted optical microscope (Axiovert 25, Zeiss) coupled with a compact USB fiber optic spectrometer (USB4000, OceanOptics). More detailed angle resolved reflectance measurements were acquired in water and controlled ethanol solutions by using a commercial Fourier

transform spectrometer (FT-66, Bruker), equipped with a homemade variable angle microreflectometer. A commercial fluidic cell was used to evaluate the sensitivity to small refractive index changes.

**Device Characterization—Photonic Module and Optoplasmonic System:** Electrical measurements on encapsulated photonic modules were performed using a standard SUSS probe station coupled to a B1500A Agilent semiconductor device analyzer. In the photonic module, either with or without any reflective coating, the OPD current in short-circuit conditions was measured during standard p-type transfer or output tests of the OLET.

In the electrical characterization of the optoplasmonic system, the OLET was driven at constant bias through a B1500A Agilent semiconductor device analyzer and the OPD photocurrent was acquired over time by an Electrochemical Workstation (Autolab/PSTAT128N+ECD module). A calibrated silicon photodiode was placed at the bottom side of the optoplasmonic system to record the OLET light passing through the glass/ITO substrate over time. The NPG surface was exposed alternatively to ultrapure water and ethanol solution at 25% and 50% in static condition. The following operational conditions were used: i) the cathode and the OLET source/OPD anode at 0 V; ii) the OLET was switched-on by keeping  $V_{\text{DS}} = V_{\text{GS}} = -20 \text{ V}$ .

In the case of interdigitated chips, two adjacent OLETs were switched on. The two OLETs shared a single drain electrode, which was located between two source electrodes. The two OPDs, which were placed on top of the two source electrodes, were kept at 0 V. Depending on the type of analysis, the OLET was kept at  $V_{\text{DS}} = V_{\text{GS}} = -20 \text{ V}$  or the  $V_{\text{GS}}$  was swept from 0 to  $-20 \text{ V}$  at  $V_{\text{DS}} = -20 \text{ V}$ .

Optical microscopy images were recorded from the top side of a photonic module encapsulated with a transparent cap by a Nikon i-80 microscope.

## Supporting Information

Supporting Information is available from the Wiley Online Library or from the author.

## Acknowledgements

M.P. and E.B. contributed equally to this work. This work received funding from the European Union's Horizon 2020 research and innovation programme under grant agreement no. 780839 (MOLOKO). The authors thank Federico Prescimone for the valuable technical support.

## Conflict of Interest

The authors declare no conflict of interest.

## Data Availability Statement

Research data are not shared.

## Keywords

nanoplasmonics, nanostructured gratings, organic light-emitting transistors, organic optical sensors, organic photodiodes, organic photonics, smart system integration

Received: May 24, 2021

Revised: July 6, 2021

Published online: August 1, 2021

- [1] C. Dincer, R. Bruch, E. Costa-Rama, M. T. Fernández-Abedul, A. Merkoçi, A. Manz, G. A. Urban, F. Güder, *Adv. Mater.* **2019**, *31*, 1806739.
- [2] A. Shakkor, J. Grant, M. Grande, D. R. S. Cumming, *Sensors* **2019**, *19*, 1715.
- [3] M. Prosa, M. Bolognesi, L. Fornasari, G. Grasso, L. Lopez-Sanchez, F. Marabelli, S. Toffanin, *Nanomaterials* **2020**, *10*, 480.
- [4] A. E. Cetin, A. F. Coskun, B. C. Galarreta, M. Huang, D. Herman, A. Ozcan, H. Altug, *Light: Sci. Appl.* **2014**, *3*, e122.
- [5] B. A. Prabowo, A. Purwidyantri, K. C. Liu, *Biosensors* **2018**, *8*, 80.
- [6] G. Schweicher, G. Garbay, R. Jouclas, F. Vibert, F. Devaux, Y. H. Geerts, *Adv. Mater.* **2020**, *32*, 1905909.
- [7] P. W. M. Blom, *Adv. Mater. Technol.* **2020**, *5*, 2000144.
- [8] M. Prosa, S. Moschetto, E. Benvenuti, M. Zambianchi, M. Muccini, M. Melucci, S. Toffanin, *J. Mater. Chem. C* **2020**, *8*, 15048.
- [9] D. Gedefaw, M. Prosa, M. Bolognesi, M. Seri, M. R. Andersson, *Adv. Energy Mater.* **2017**, *7*, 1700575.
- [10] L. Bürgi, R. Pfeiffer, M. Mücklich, P. Metzler, M. Kiy, C. Winnewisser, *Org. Electron.* **2006**, *7*, 114.
- [11] T. Kamada, R. Hatsumi, K. Watanabe, S. Kawashima, M. Katayama, H. Adachi, T. Ishitani, K. Kusunoki, D. Kubota, S. Yamazaki, *J. Soc. Inf. Disp.* **2019**, *27*, 361.
- [12] C. M. Lochner, Y. Khan, A. Pierre, A. C. Arias, *Nat. Commun.* **2014**, *5*, 5745.
- [13] A. K. Bansal, S. Hou, O. Kulyk, E. M. Bowman, I. D. W. Samuel, *Adv. Mater.* **2015**, *27*, 7638.
- [14] H. Lee, E. Kim, Y. Lee, H. Kim, J. Lee, M. Kim, H. J. Yoo, S. Yoo, *Sci. Adv.* **2018**, *4*, eaas9530.
- [15] Y. Khan, D. Han, A. Pierre, J. Ting, X. Wang, C. M. Lochner, G. Bovo, N. Yaacobi-Gross, C. Newsome, R. Wilson, A. C. Arias, *Proc. Natl. Acad. Sci. USA* **2018**, *115*, E11015.
- [16] Y. Khan, D. Han, J. Ting, M. Ahmed, R. Nagisetty, A. C. Arias, *IEEE Access* **2019**, *7*, 128114.
- [17] E. L. Ratcliff, P. A. Veneman, A. Simmonds, B. Zacher, D. Huebner, S. S. Saavedra, N. R. Armstrong, *Anal. Chem.* **2010**, *82*, 2734.
- [18] D. Threm, Y. Nazirizadeh, A. Pradana, M. Rädler, J. Mikat, M. Gerken, in *16th Int. Conf. on Optical MEMS and Nanophotonics*, IEEE, Piscataway, NJ **2011**, pp. 113–114.
- [19] F. Lefèvre, A. Chalifour, L. Yu, V. Chodavarapu, P. Juneau, R. Izquierdo, *Lab Chip* **2012**, *12*, 787.
- [20] R. Liu, T. Xiao, W. Cui, J. Shinar, R. Shinar, *Anal. Chim. Acta* **2013**, *778*, 70.
- [21] B. Lamprecht, T. Abel, E. Kraker, A. Haase, C. Konrad, M. Tscherner, S. Köstler, H. Ditlbacher, T. Mayr, *Phys. Status Solidi RRL* **2010**, *4*, 157.
- [22] K. S. Nalwa, Y. Cai, A. L. Thoeming, J. Shinar, R. Shinar, S. Chaudhary, *Adv. Mater.* **2010**, *22*, 4157.
- [23] G. Williams, C. Backhouse, H. Aziz, *Electronics* **2014**, *3*, 43.
- [24] F. Elsammah, A. Bilgaiyan, M. Affiq, C. H. Shim, H. Ishidai, R. Hattori, *Biosensors* **2019**, *9*, 48.
- [25] A. Shakkor, B. C. Cheah, M. A. Al-Rawhani, M. Grande, J. Grant, L. C. P. Gouveia, D. R. S. Cumming, *IEEE Sens. J.* **2018**, *18*, 9188.
- [26] S. Joshi, A. Segarra-Fas, J. Peters, H. Zuilhof, T. A. Van Beek, M. W. F. Nielen, *Analyst* **2016**, *141*, 1307.
- [27] S. Giudicatti, F. Marabelli, P. Pellacani, *Plasmonics* **2013**, *8*, 975.
- [28] B. Bottazzi, L. Fornasari, A. Frangolho, S. Giudicatti, A. Mantovani, F. Marabelli, G. Marchesini, P. Pellacani, R. Therisod, A. Valsesia, *J. Biomed. Opt.* **2014**, *19*, 017006.
- [29] J. Frischeisen, C. Mayr, N. A. Reinke, S. Nowy, W. Brütting, *Opt. Express* **2008**, *16*, 18426.
- [30] R. B. M. Schasfoort, J. A. Marquart, H. Zhao, P. Schuck, E. T. Gedig, R. Karlsson, O. Karlsson, P. Belcher, K. Wagner, N. T. Ditto, J. Eckman, D. Apiyo, S. D. Vallet, L. Deddens, A. Vonarburg, R. Salza, C. Faye, A. Aranyos, N. Thierry-Mieg, S. Ricard-Blum, in *Handbook of Surface Plasmon Resonance*, 2nd ed. (Ed: R. B. M. Schasfoort), The Royal Society of Chemistry, London **2017**, Ch. 1.
- [31] R. Capelli, S. Toffanin, G. Generali, H. Usta, A. Facchetti, M. Muccini, *Nat. Mater.* **2010**, *9*, 496.
- [32] M. Muccini, W. Koopman, S. Toffanin, *Laser Photonics Rev.* **2012**, *6*, 258.
- [33] M. Muccini, S. Toffanin, *Organic Light-Emitting Transistors: Towards the Next Generation Display Technology*, John Wiley & Sons, Hoboken, NJ **2016**.
- [34] C. K. Renshaw, X. Xu, S. R. Forrest, *Org. Electron.* **2010**, *11*, 175.
- [35] X. Tong, S. R. Forrest, *Org. Electron.* **2011**, *12*, 1822.
- [36] K. Swathi, K. S. Narayan, *Appl. Phys. Lett.* **2016**, *109*, 193302.
- [37] Y. Lin, J. Chen, M. M. Tavakoli, Y. Gao, Y. Zhu, D. Zhang, M. Kam, Z. He, Z. Fan, *Adv. Mater.* **2019**, *31*, 1804285.
- [38] H. Wang, H. Liu, Q. Zhao, C. Cheng, W. Hu, Y. Liu, *Adv. Mater.* **2016**, *28*, 624.
- [39] C. W. Chu, C. W. Chen, S. H. Li, E. H. E. Wu, Y. Yang, *Appl. Phys. Lett.* **2005**, *86*, 253503.
- [40] Q. Li, S. Bi, K. Asare-Yeboah, J. Na, Y. Liu, C. Jiang, J. Song, *ACS Nano* **2019**, *13*, 8425.
- [41] S. Bi, Q. Li, Z. He, Q. Guo, K. Asare-Yeboah, Y. Liu, C. Jiang, *Nano Energy* **2019**, *66*, 104101.
- [42] Y. Sun, C. Borek, K. Hanson, P. I. Djurovich, M. E. Thompson, J. Brooks, J. J. Brown, S. R. Forrest, *Appl. Phys. Lett.* **2007**, *90*, 10.
- [43] C. Borek, K. Hanson, P. I. Djurovich, M. E. Thompson, K. Aznavour, R. Bau, Y. Sun, S. R. Forrest, J. Brooks, L. Michalski, J. Brown, *Angew. Chem.* **2007**, *119*, 1127.
- [44] M. Ullah, R. Wawrzinek, F. Maasoumi, S. Lo, E. B. Namdas, *Adv. Opt. Mater.* **2016**, *4*, 1022.
- [45] M. Prosa, E. Benvenuti, M. Pasini, U. Giovannella, M. Bolognesi, L. Meazza, F. Galeotti, M. Muccini, S. Toffanin, *ACS Appl. Mater. Interfaces* **2018**, *10*, 25580.
- [46] S. Toffanin, R. Capelli, W. Koopman, G. Generali, S. Cavallini, A. Stefani, D. Saguatti, G. Ruani, M. Muccini, *Laser Photonics Rev.* **2013**, *7*, 1011.
- [47] M. Natali, S. D. Quiroga, L. Passoni, L. Criante, E. Benvenuti, G. Bolognini, L. Favaretto, M. Melucci, M. Muccini, F. Scotognella, F. Di Fonzo, S. Toffanin, *Adv. Funct. Mater.* **2017**, *27*, 1605164.
- [48] S. Döring, T. Otto, M. Cehovski, O. Charfi, R. Caspary, W. Kowalsky, T. Rabe, *Phys. Status Solidi A* **2016**, *213*, 2387.
- [49] B. Siegmund, A. Mischok, J. Benduhn, O. Zeika, S. Ullbrich, F. Nehm, M. Böhm, D. Spoltore, H. Fröb, C. Körner, K. Leo, K. Vandewal, *Nat. Commun.* **2017**, *8*, 15421.
- [50] S. Ullbrich, B. Siegmund, A. Mischok, A. Hofacker, J. Benduhn, D. Spoltore, K. Vandewal, *J. Phys. Chem. Lett.* **2017**, *8*, 5621.
- [51] J. E. Troyan, *J. Am. Chem. Soc.* **1942**, *64*, 3056.
- [52] H. Chen, W. Huang, T. J. Marks, A. Facchetti, H. Meng, *Small* **2021**, *17*, 2007661.
- [53] H. I. Un, J. Y. Wang, J. Pei, *Adv. Sci.* **2019**, *6*, 1900375.